SCIENCE CHINA PRESS

SCIENCE CHINA Life Sciences
life.scichina.com link.springer.com
https://doi.org/10.1007/s11427-025-3252-6

RESEARCH PAPER

Food processing-derived carbon dots disrupt male fertility via the gut-testis axis

Peigen Chen[1,2,3†], Menghui Ma[1,2,3†], Yanqing Li[1,2,3†], Xi Chen[4,5], Zhenhan Xu[1,2,3], Jintao Guo[1,2,3], Xinyi Hu[4,5], Linyan Lv[1,2,3], Jianhe Guo[4,5*] & Guihua Liu[1,2,3*]

[1]Reproductive Medicine Center, The Sixth Affiliated Hospital, Sun Yat-sen University, Guangzhou 510655, China
[2]Guangdong Engineering Technology Research Center of Fertility Preservation, Guangzhou 510655, China
[3]Biomedical Innovation Center, The Sixth Affiliated Hospital, Sun Yat-sen University, Guangzhou 510655, China
[4]Guangdong Provincial Key Laboratory of Sensing Technology and Biomedical Instrument, Guangzhou 510655, China
[5]School of Biomedical Engineering, Shenzhen Campus of Sun Yat-sen University, Shenzhen 518083, China

†Contributed equally to this work
*Corresponding authors (Guihua Liu, email: liuguihua@mail.sysu.edu.cn; Jianhe Guo, email: guojianhe@mail.sysu.edu.cn)

Received 8 August 2025; Accepted 4 February 2026; Published online 20 May 2026

Carbon dots (CDs) are unintentionally formed during thermal processing of food and are emerging environmental pollutants that may pose health risks. We investigated the reproductive toxicity of food-derived CDs via the gut-testicular axis by exposing male mice to environmentally relevant doses (25 and 100 mg kg^{-1} d^{-1}) for 15 weeks. Multi-omics analysis (including metagenomics, transcriptomics, and metabolomics) revealed that CDs significantly altered the gut microbiota composition, reducing beneficial bacteria (*Akkermansia muciniphila*, $P<0.01$) while increasing pathogenic bacteria (Desulfovibrionaceae, $P<0.001$). Functional analysis revealed upregulation of the lipopolysaccharide (LPS) biosynthesis pathway ($P<0.001$) and reduced levels of barrier-protective tryptophan metabolites. Time-series studies established a mechanistic sequence: microbiota disruption (days 1–3), intestinal barrier dysfunction (days 3–5), blood-testis barrier damage (days 5–7), testicular inflammation, and reproductive dysfunction. Dose-dependent testicular toxicity included reduced testosterone synthesis ($P<0.001$), impaired spermatogonial stem cell maintenance due to downregulation of PLZF, and impaired fertility. Testicular transcriptomics analysis revealed activation of the IL-17 signaling pathway and inhibition of steroidogenesis. This study provides comprehensive evidence that CD induces male reproductive toxicity through microbiota-dependent mechanisms, emphasizing the environmental health implications of dietary nanoparticle exposure.

carbon dots | male infertility | gut microbiota | reproductive toxicology | nanomaterial toxicity

INTRODUCTION

Over the past five decades, male fertility has declined by more than 50%, with global sperm concentration plummeting from 104 million per milliliter in 1973 to 49 million per milliliter in 2018—a staggering 51.6% decline that is accelerating at a rate of 1.2% per year (Levine et al., 2023). While environmental toxins have long been suspected as the culprits behind this reproductive disaster, a hidden class of pollutants may be quietly infiltrating our daily diets: food-derived carbon dots (CDs). These nanoscale particles are now widespread throughout the global food supply chain, including carbonated soft drinks (3%–5% concentration) (Li et al., 2018), roast duck (Cong et al., 2018), honey (Mandani et al., 2017), salmon (Song et al., 2019), beer (Wang et al., 2015), and bread (Sk et al., 2012), and have undergone virtually no reproductive health safety assessments.

Carbon dots are fluorescent nanoparticles with diameters less than 10 nm that spontaneously form during thermal food processing—from bread baking to coffee roasting—creating a vast and unmonitored source of human exposure (Singh et al., 2024). Recent surveys indicate carbon dot concentrations in various foods range from 0.1 to 50 mg kg^{-1}, with human daily exposure levels of 0.5–2.0 mg kg^{-1} of body weight (Das et al., 2025). Unlike intentionally added food additives, CDs formed during processing, despite their widespread presence and concerning biological activity (including cellular uptake, oxidative stress induction, and inflammatory responses), have not yet undergone regulatory review (Sharma et al., 2024). The current regulatory framework remains fragmented and fails to address the toxicological characteristics of nanoparticles in food matrices (Gupta et al., 2024).

The gastrointestinal tract serves as a critical interface between ingested CDs and systemic circulation, while the gut-testis axis represents a particularly vulnerable pathway for reproductive toxicity (Zhang et al., 2023). This bidirectional network linking the gut microbiota to male reproductive function operates

Citation: Chen, P., Ma, M., Li, Y., Chen, X., Xu, Z., Guo, J., Hu, X., Lv, L., Guo, J., and Liu, G. (2026). Food processing-derived carbon dots disrupt male fertility via the gut-testis axis. Sci China Life Sci 69, 3112–3126. https://doi.org/10.1007/s11427-025-3252-6

CrossMark click for updates

through gut barrier integrity, microbial metabolite production, and inflammatory control—all of which are disrupted by nanoparticle exposure (Al-Asmakh et al., 2014; Torres et al., 2018). Increasing evidence suggests that gut microbiota dysbiosis disrupts the blood-testis barrier through lipopolysaccharide (LPS)-mediated inflammatory cascades, thereby profoundly affecting testosterone production and sperm quality (Ding et al., 2020; Esterházy et al., 2019). However, the mechanism by which nanoparticles in food utilize this pathway remains unexplored.

To address this critical knowledge gap, this study integrated multi-omics approaches to conduct a comprehensive investigation of the reproductive toxicology of CD. Through transcriptomics, microbiomics, and metabolomics analyses, we mapped the complete pathway from oral CD exposure to testicular dysfunction. This study validated the core hypothesis that CD in food disrupts male fertility through a sequential cascade mechanism. Through time-series experiments, we established the temporal dynamics of this toxic pathway and identified key intervention nodes.

RESULTS

Carbon dots induce dose-dependent reproductive toxicity through gut-mediated mechanisms

The overall design of the study is shown in Figure 1A. To establish the foundation for our mechanistic studies, we first characterized the carbon dots in food and confirmed their reproductive toxicity. High-resolution transmission electron microscopy (HRTEM) revealed that these nanoparticles were spherical, with uniform morphology and an average diameter of (3.8±0.5) nm (Figure 1B) and exhibited characteristic blue-green fluorescence emission under excitation at 280–300 nm (Figure 1C). Dynamic light scattering measurements revealed a zeta potential of (−18.3±2.7) mV, confirming moderate colloidal stability under physiological conditions. These physicochemical properties indicate that the extracted particles are genuine food-derived carbon dots, comparable to those previously reported in carbonated beverages.

The high-dose CD (HCD) group exhibited significantly reduced body weight gain ($P<0.01$, Figure 1D) and marked testicular atrophy (Figure 1E), accompanied by functional defects, including a 35% reduction in serum testosterone levels ($P<0.001$; Figure 1G) and significantly reduced fertility, manifested as reduced litter size in mating tests (Figure 1F). At the molecular level, CD exposure significantly reduced the expression of promyelocytic leukemia zinc finger protein (*Plzf*), a key regulator of spermatogonial stem cells (Figure 1H), and disrupted multiple aspects of spermatogenesis, including chromosome structure, RNA processing, and sperm maturation (Figure 1I; Figure S1). The marked dose-dependent nature of these effects, where HCD consistently caused more severe damage than low-dose CD (LCD), suggests that CD in food at environmentally relevant exposure levels can impair male reproductive function.

Gut microbiota dysbiosis emerges as a key mechanism

After establishing reproductive toxicity, we further investigated whether gut microbiota dysbiosis acted as an initiating mechanism. Metagenomic sequencing results revealed that CD exposure fundamentally altered the structure of the gut microbiota. α diversity (Shannon index and Simpson index) remained relatively stable across groups (Figure 2A). β diversity analysis indicated that the community composition of mice in the CD exposure group differed significantly from that of the control group (ANOSIM: $R=0.612$, $P=0.001$; Figure 2B and C). This community restructuring exhibited a characteristic pattern of significant reduction in beneficial bacterial genera and significant expansion of pathogenic bacterial genera.

Classification composition analysis showed significant changes at both the phylum (Figure 2D) and species (Figure 2E) levels. Overlay plots visually demonstrated the extent of community restructuring between different treatment groups, indicating fundamental disruption of ecosystem stability. Most critically, CD exposure led to a significant reduction in beneficial bacterial species (including *Akkermansia muciniphila*, *Acidaminococcus* sp., and *Bacteroides caecimuris*) ($P<0.01$) while promoting the significant expansion of potential pathogenic bacteria (such as Desulfovibrionaceae *LT0009* and *Mailhella* sp.) ($P<0.001$) (Figure 2F).

Beyond taxonomic changes, functional metagenomic analysis revealed the mechanistic significance of these microbial alterations. CD exposure significantly upregulated genes associated with LPS biosynthesis and bacterial quorum sensing ($P<0.001$), while suppressing pathways related to beneficial metabolites (including short-chain fatty acids, tryptophan metabolism, and steroid hormone synthesis) (Figure 2G). The expression of LpxC, a rate-limiting enzyme in the LPS biosynthesis pathway, was significantly up-regulated and strongly positively correlated with pathogenic bacteria, while negatively correlated with beneficial bacterial species (Figure 2H).

Detailed functional pathway analysis (Figure S2) provided comprehensive mechanistic insights into the metabolic dysregulation underlying CD-induced gut microbiota dysbiosis. The LPS biosynthesis pathway showed coordinated upregulation of multiple enzymatic steps, with CPG-phosphoglucose isomerase activity significantly increased in a dose-dependent manner ($P<0.001$) (Figure S2B). Upstream metabolic precursors were also significantly elevated, including glycerol-3-phosphate ($P<0.01$) and D-glucose ($P<0.01$) (Figure S2C), indicating that the metabolic flux entering LPS biosynthesis via the fructose and mannose metabolic pathways was significantly enhanced (Figure S2A).

In contrast, the tryptophan metabolic pathway exhibited significant inhibition at multiple enzymatic steps (Figure S2D). Indole production catalyzed by tryptophanase (tnaA) significantly decreased from the control group level to LCD ($P<0.0001$) and HCD ($P<0.0001$). The tryptophan metabolic pathway, which converts tryptophan into L-tryptophan via tryptophan B, also showed similar dose-dependent inhibition ($P<0.001$). Most critically, the terminal step of oxaloacetic acid synthesis via DLD and ECH1 enzymes was severely impaired ($P<0.001$), indicating disrupted tryptophan metabolism and reduced synthesis of protective metabolites. Detailed analysis of functional genes associated with tryptophan metabolism revealed significant dose-dependent inhibition in the CD-exposed group ($P<0.001$), and a strong correlation between tryptophanase activity and the abundance of beneficial bacteria, elucidating the mechanistic basis for reduced synthesis of protective indole metabolites (Figure 2I). These functional alterations ultimately led to significantly elevated fecal endotoxin (LPS) levels in the LCD

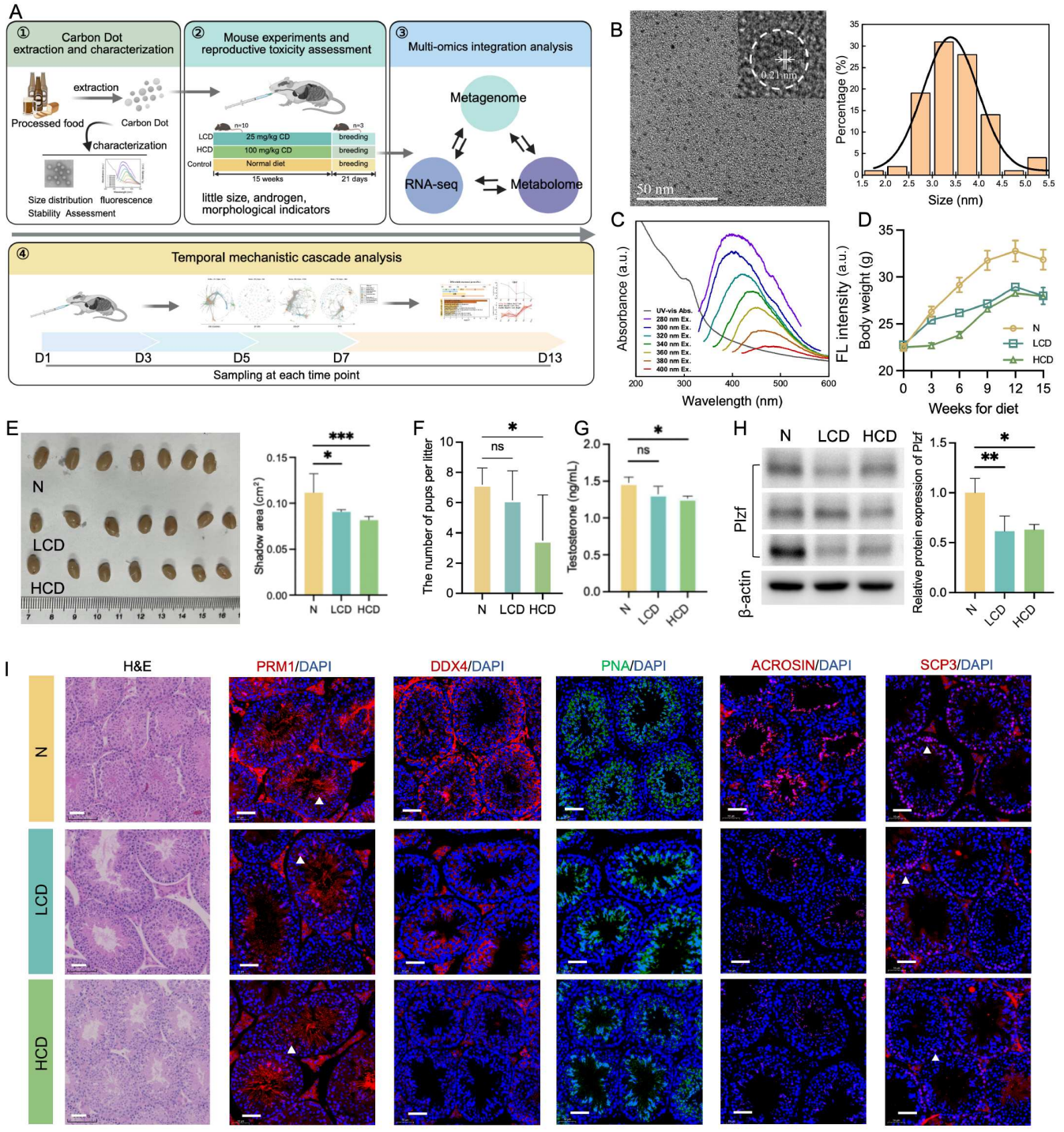


Figure 1. Chronic exposure to foodborne carbon dots impairs testicular function in mice. A, Experimental design timeline for 15-week CD exposure. B, High-resolution TEM images (left) and size distribution histogram (right) of foodborne CDs extracted from carbonated beverages. Scale bar: 50 nm. C, Fluorescence emission spectra of CDs (0.1 mg mL^{-1} in ultrapure water) under varying excitation wavelengths (280–500 nm). D, Body weight trajectories of control (N), LCD, and HCD groups over 15 weeks. E, Representative images of testes and quantitative analysis of testicular projected area. F, Litter size distribution from mating experiments. G, Serum testosterone levels measured by ELISA. H, Western blot analysis of PLZF protein expression in testicular tissues. I, Histological evaluation: H&E staining of testis (left) and immunofluorescence detection of spermatogenesis markers (*DDX4*, *PNA*, *ACROSIN*, *PRM1*, *SCP3*; scale bars: 50 μm). Data are mean±SEM; **P*<0.05, ***P*<0.01, ****P*<0.001 *vs.* control (one-way ANOVA with Tukey's test).

group (*P*<0.01) and HCD group (*P*<0.001) compared to the control group (Figure 2J), establishing a key association between CD exposure, gut microbiota dysbiosis, and increased endotoxin production.

Gut barrier dysfunction triggers systemic inflammatory cascade

CD-induced microbiota dysbiosis and excessive endotoxin (LPS) production facilitate systemic toxicity through intestinal barrier

https://doi.org/10.1007/s11427-025-3252-6

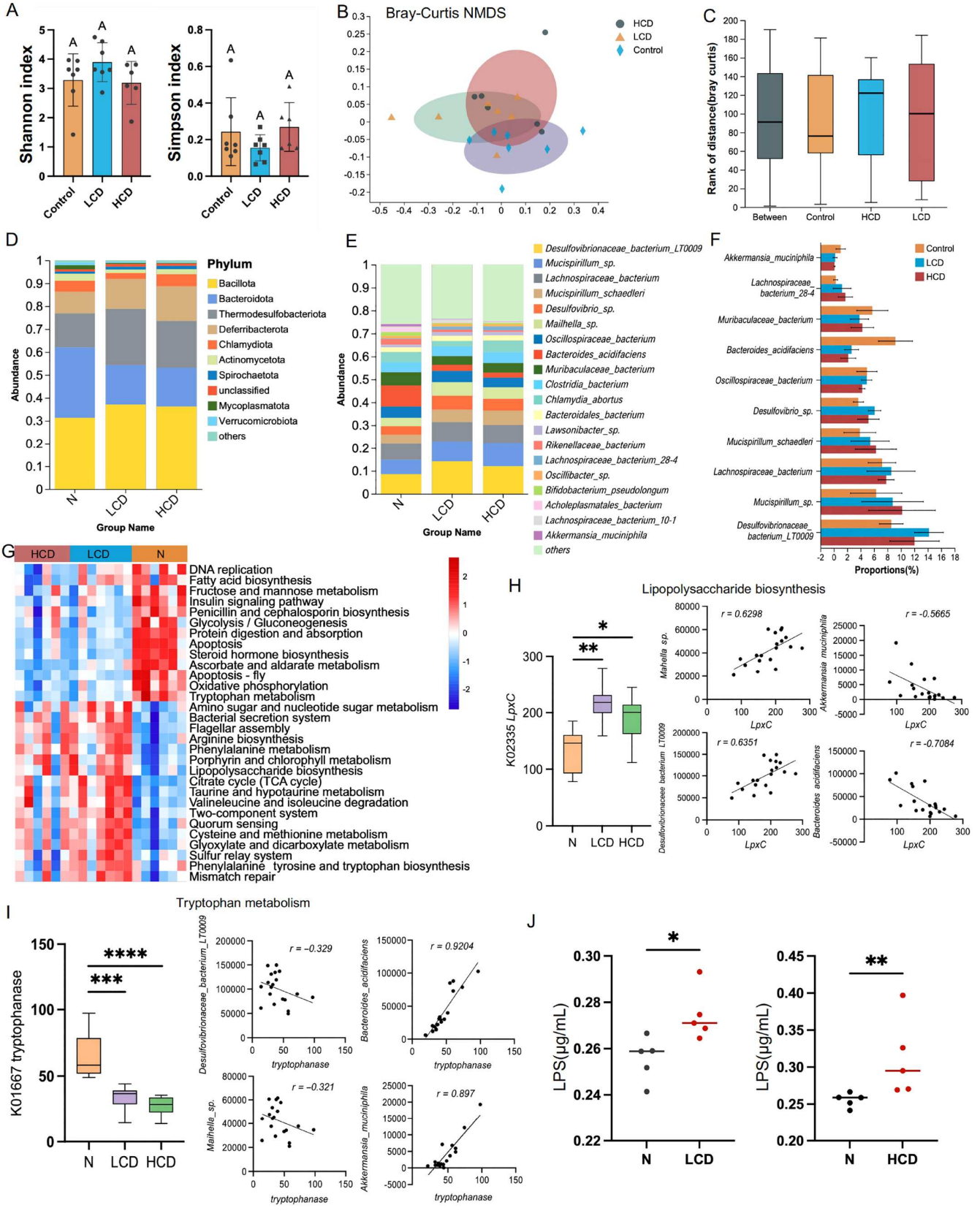


Figure 2. Foodborne CDs induce gut microbiota dysbiosis and LPS biosynthesis. A, NMDS analysis of gut microbiota beta diversity. B, Bray-Curtis distance matrix between groups. C, ANOSIM test for group dissimilarity. D, Phylum-level taxonomic composition. E, Microbial co-occurrence networks (nodes: species; edges: $|r|>0.4$). F, Differential abundance of key taxa ($\log_2$ fold change). G, Heatmap of functional pathway activity (z-score normalized). H, Expression levels of LPS biosynthesis gene *lpxC*. I, Correlation heatmap between tryptophan metabolism genes and microbiota taxa. J, Fecal LPS quantification by ELISA. Data: mean±SEM; **P*<0.05, ***P*<0.01, ****P*<0.001.

dysfunction. Metabolomics analysis provided robust evidence for this barrier dysfunction, revealing unique metabolite profiles in the gut (Figure 3A) and circulatory system (Figure 3B) of CD-exposed mice. Gut metabolomics showed dose-dependent alterations in gut metabolite profiles, with a distinct separation between the control and CD-exposed groups, and significant changes in microbial-derived compounds and metabolic intermediates (Figure 3C). Most notably, the gut and blood metabolome profiles of control mice remained distinct, while those of CD-exposed mice showed significant similarity (Figure 3D), indicating increased intestinal permeability and the entry of gut-derived metabolites into the systemic circulation.

Histological examination confirmed this "leaky gut" phenotype, with PAS staining showing a significant thinning of the mucous layer, and immunohistochemical results indicating that the expression of tight junction protein occludin was significantly reduced in both the LCD and HCD groups (Figure 3E). The impaired intestinal barrier led to systemic endotoxemia, characterized by elevated levels of LPS in the circulation and altered serum metabolite profiles, including reduced levels of protective indole compounds ($P<0.001$) and increased levels of pro-inflammatory lipid mediators such as arachidonic acid, linoleic acid, and adrenaline ($P<0.01$) (Figure 3F). Further inspection of individual metabolites showed that serum arachidonic acid was significantly elevated in a dose-dependent manner in CD-exposed mice, whereas fecal arachidonic acid exhibited an overall decreasing trend, consistent with enhanced luminal-to-systemic flux of this pro-inflammatory lipid mediator (Figure S3A and B). Beyond tryptophan, we also noted pronounced alterations in fecal purine- and pyrimidine-related nucleosides and nucleobases (e.g., thymidine, cytidine, guanine and deoxyguanosine), with concordant but less marked trends in serum (Figure S3C and D), suggesting that CDs induce broader remodeling of nucleotide metabolism along the gut-systemic axis.

This systemic inflammatory state disrupts the blood-testis barrier (BTB), creating conditions conducive to reproductive toxicity. Immunohistochemical analysis revealed significant impairment of key BTB components, including *N-cadherin*, *β-catenin*, and *occludin*, in CD-exposed mice (Figure 3G). Integrated pathway analysis identified tryptophan metabolism, gluconeogenesis, and glycolysis as core pathways linking gut microbiota alterations to testicular dysfunction (Figure 3H), providing a theoretical basis for the mechanism by which CD-induced microbiota dysbiosis transmits its effects to the reproductive system via systemic inflammatory mediators.

Blood-testis barrier compromise enables testicular inflammatory damage

Comprehensive RNA sequencing analysis of testicular tissue revealed distinct molecular mechanisms underlying CD-induced reproductive dysfunction. Principal component analysis (PCA) clearly distinguished CD-exposed groups from controls (Figure 4A), with ternary plot analysis revealing treatment-specific gene expression patterns (Figure 4B). Cell type decomposition analysis identified macrophages as the most sensitive population, with functional scores significantly decreased in LCD (3.96 ± 0.23, $P<0.01$) and HCD groups (3.67 ± 0.15, $P<0.001$) compared to controls (4.51 ± 0.63) (Figure 4C). Macrophage polarization analysis revealed that the canonical M1 (pro-inflammatory) gene signature declined modestly from control (4.4) through LCD (3.6) to HCD (3.5), whereas the M2-associated signature remained relatively stable (5.3–5.4) (Figure S4A–D).

Gene expression trend analysis identified six distinct clusters, with progressively upregulated genes (Cluster 5) enriched in the TLR4 signaling pathway, providing molecular evidence for LPS-mediated inflammation, while downregulated genes (Cluster 4) were enriched in monocyte migration regulation (Figure 4D). Key gene analysis revealed unchanged StAR mRNA but significantly downregulated Hsd3b1 in the HCD group, suggesting post-transcriptional testosterone synthesis impairment. Inflammatory markers Tlr4 and Il1b showed dose-dependent upregulation, while Cyp17a1 was significantly inhibited (Figure 4E).

Protein validation confirmed transcriptomic findings: StAR protein was significantly reduced despite unchanged mRNA levels, while IL-17A protein was elevated in both treatment groups, establishing IL-17A as a key inflammatory mediator (Figure 4F). Oxidative stress analysis revealed significant down-regulation of antioxidant enzymes, including catalase, Hmox1, and Txn1, in the HCD group (Figure S4).

Time-course analysis establishes gut microbiota disruption as the initiating event in reproductive toxicity

To establish the causal relationship within the gut-testicular axis mechanism we proposed, we conducted high-resolution time-series analysis, simultaneously tracking changes in gut microbiota following CD exposure and testicular responses (Figure 5A). The time-series analysis provided strong evidence that gut microbiota dysbiosis serves as the initiating event. Metagenomic analysis revealed rapid and dynamic changes in the gut microbiota, with the most significant shifts in community structure occurring between 1- and 3-day post-exposure (ANOSIM: $R=0.78$, $P<0.001$; Figure 5B and C). α diversity exhibited a typical biphasic response, with a significant increase on day 3 ($P<0.01$), followed by a gradual decline on days 5, 7, and 13 (Figure 5D), suggesting that CD-resistant microorganisms were gradually selected after initial ecological disturbance. Microbial network analysis revealed that the coexistence network fragmented gradually from days 1 to 3, followed by reorganization into a significantly altered community structure from days 5 to 7 (Figure 5E).

In sharp contrast to these early microbial changes, transcriptomic analysis of testicular tissue revealed no significant changes in gene expression within the first 5 days post-exposure (Figure 5F). The first detectable changes in the testicular transcriptome appeared on day 7, with 173 differentially expressed genes identified between days 5 and 7 (Figure 5G), primarily affecting the cytoplasmic translation and oxidative phosphorylation pathways, indicative of early cellular stress responses(Figure 5H).

Most importantly, the temporal analysis of key barrier integrity and inflammatory markers established a precise time sequence between gut microbiota dysbiosis and testicular inflammation. Gap junction beta 2 (GJB2, connexin 26), a gap junction protein that mediates communication between Sertoli cells and developing germ cells rather than forming the tight junction core of the blood-testis barrier, remained stable from days 1 to 3 but showed a sharp decline from days 3 to 5 (Figure 5I). Subsequently, from days 5 to 7, LPS response genes (including Toll-like receptor 4 (Tlr4) and interleukin-17 receptor A (Il17ra)) were significantly upregulated (Figure 5J), consistent

https://doi.org/10.1007/s11427-025-3252-6

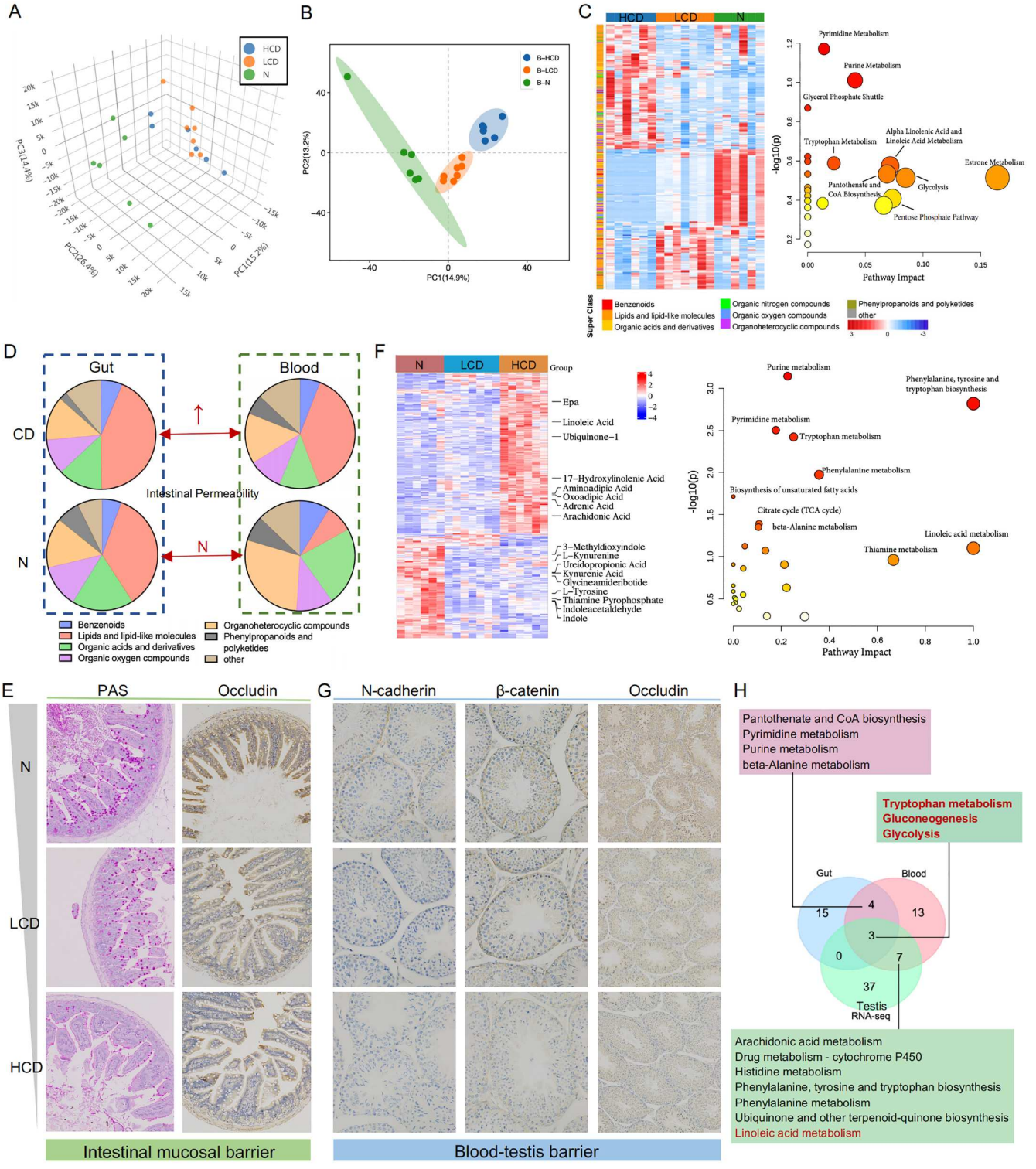


Figure 3. Metabolic dysregulation and barrier dysfunction in the gut-testis axis. A and B, PLS-DA analysis of gut metabolomics (A, 3D plot) and serum metabolomics (B, 2D plot) revealed distinct clustering patterns among different treatment groups. C, Heatmap of gut metabolite differential abundance, accompanied by pathway enrichment analysis (right panel). D, Comparison of superclass distribution of gut metabolites and blood metabolites among different treatment groups (pie chart). E, Intestinal barrier assessment: PAS staining (mucus, magenta) and occludin immunohistochemistry (brown) show thinning of the mucus layer and disruption of tight junctions. F, Heatmap of serum metabolites with differential abundance, accompanied by enriched metabolic pathway analysis (right panel). G, Assessment of blood-testis barrier integrity via immunohistochemistry of key junctional proteins (N-cadherin, β-catenin, occludin). H, Integrated multi-omics pathway analysis linking gut microbiota, metabolomics, and testis transcriptomics data. Scale bar: 100 μm.

with the notion that early disruption of Sertoli-germ cell communication precedes or coincides with the breakdown of Sertoli-Sertoli tight junctions that constitute the structural BTB. This precisely defined temporal sequence (microbiota dysregu-

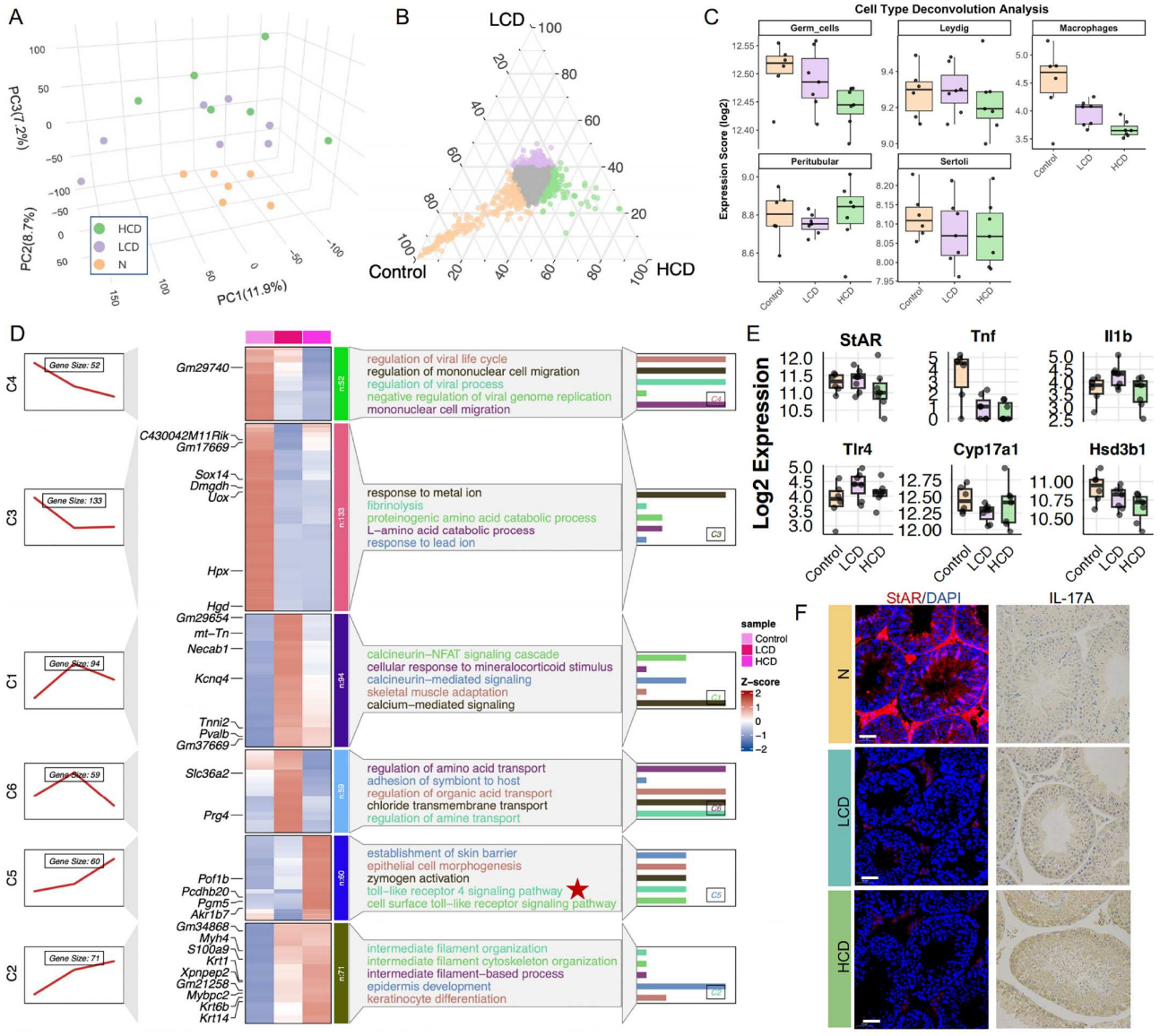


Figure 4. Testicular transcriptomic analysis reveals inflammatory activation and steroid production disorders. A, PCA of the testicular transcriptome shows a clear separation between the control group and the CD-exposed group. B, A ternary plot analysis demonstrates treatment-specific gene expression patterns across the three experimental groups. C, Cell type decomposition analysis shows a dose-dependent decrease in macrophage function scores in the CD-exposed group. D, Gene expression trend analysis identifies six distinct co-expression clusters, with Cluster 5 (upregulated) enriched for the TLR4 signaling pathway and Cluster 4 (downregulated) enriched for the monocyte migration regulation pathway. E, Key gene expression levels involved in steroidogenesis (*StAR*, *Hsd3b1*, *Cyp17a1*) and inflammation (*Tlr4*, *Il1b*) showed dose-dependent changes. F, Protein expression was validated via immunofluorescence (StAR) and immunohistochemistry (IL-17A), confirming reduced StAR protein expression and elevated IL-17A levels in testicular tissue.

lation (days 1–3) → blood-testis barrier dysfunction (days 3–5) → inflammation activation (days 5–7) → reproductive dysfunction (after day 7)) and provides evidence that microbiota dysregulation is the initiating event of CD-induced reproductive toxicity. The temporal misalignment between microbial changes and testicular effects clearly establishes a causal relationship within the proposed gut-testis axis mechanism, indicating that CD-induced reproductive damage is mediated through a microbiota-dependent pathway rather than direct gonadal toxicity.

FMT confirms the causal role of gut microbiota in reproductive toxicity

To establish causality beyond temporal correlation, we performed bidirectional fecal microbiota transplantation (FMT) experiments. Comprehensive sperm parameter analysis using computer-assisted sperm analysis (CASA) revealed that CD exposure significantly impaired multiple sperm quality parameters: sperm concentration decreased by 59.1% ($(27.4\pm7.4)\times10^6$ to $(11.2\pm4.1)\times10^6$ mL^{-1}, P=0.005), motile sperm percentage decreased by 37.3% (58.4%±8.4% to 36.6%±10.6%, P=0.008), and progressive motility decreased by 44.6% (24.2%±7.4% to 13.4%±3.4%, P=0.028) compared with controls (Figure S5).

Transplanting fecal microbiota from CD-treated mice to normal mice successfully reproduced the key features of reproductive damage: sperm concentration decreased by 42.5% (P=0.021), motile sperm by 33.2% (P=0.008), progressive motility by 38.8% (P=0.045), and rapid motility by 46.7% (P=0.045) compared

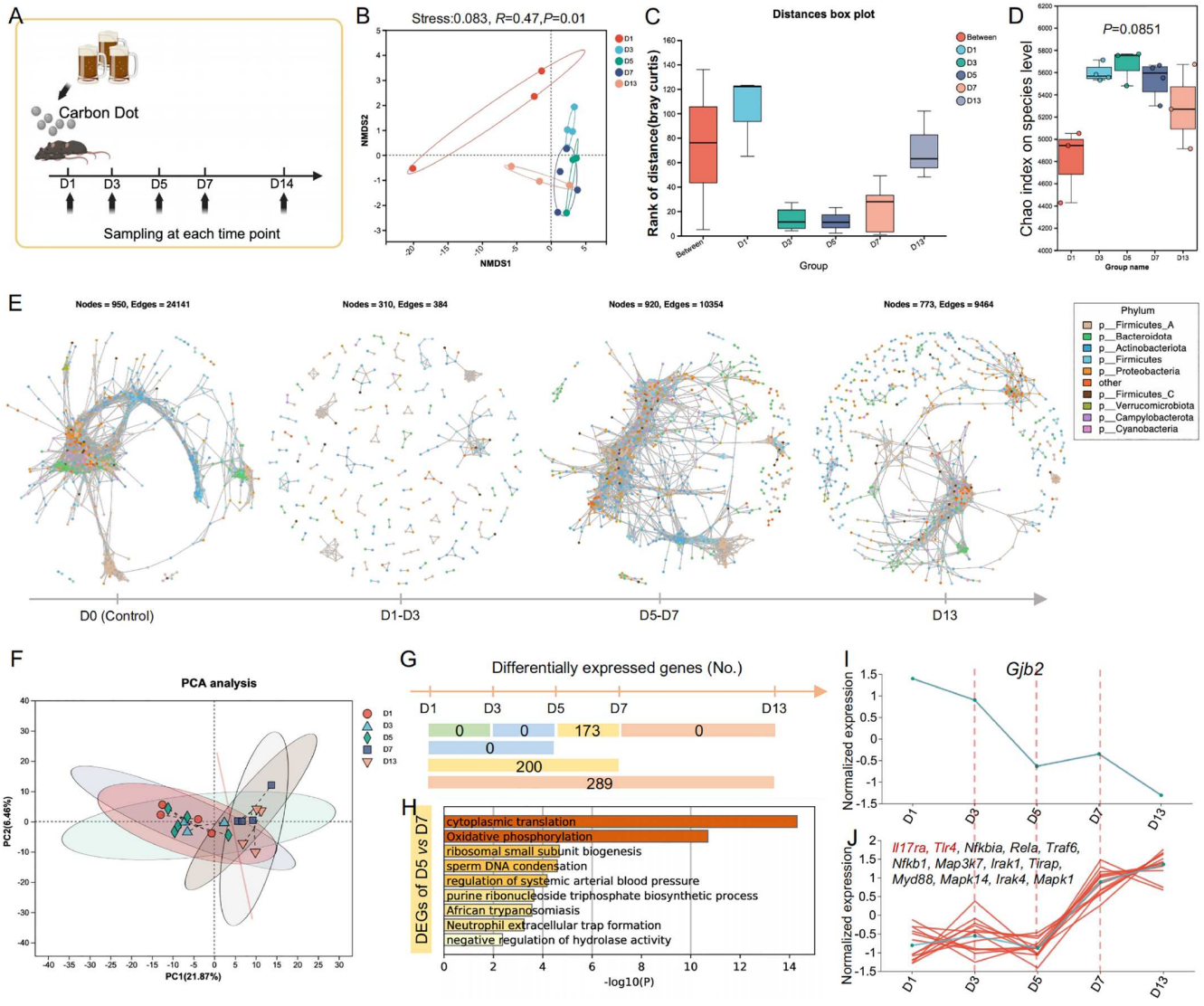


Figure 5. Temporal dynamics of gut-testis axis disruption post-CD exposure. A, Time-series experimental design showing sampling time points at days 1, 3, 5, 7, and 13 post-CD exposure for integrated gut microbiota and testis transcriptome analysis. B, Shannon diversity index of gut microbiota showing a biphasic response, i.e., initial increase followed by gradual decline. C, Non-metric multidimensional scaling (NMDS) plot showing progressive changes in microbial community structure over time. D, ANOSIM analysis confirmed significant temporal intergroup differences (R=0.78, P<0.001). E, Microbial co-occurrence network showing community fragmentation (days 1–3) followed by reorganization (days 5–7) with reduced connectivity. F, PCA of the testis transcriptome shows a delayed onset of gene expression changes, beginning on day 7. G, Counts of differentially expressed genes between consecutive time points show minimal changes until day 7 (173 differentially expressed genes between D5 and D7). H, Gene Ontology enrichment analysis comparing D5 and D7 highlights cytoplasmic translation and oxidative phosphorylation pathways as early stress responses. I, The spatiotemporal expression profile of gap junction protein Gjb2 shows stability (days 1–3) followed by a sharp decline (days 3–5), indicating blood-testis barrier dysfunction. J, The expression dynamics of LPS-responsive genes (*Tlr4*, *Il17ra*) show delayed inflammatory activation following barrier damage (days 5–7).

with controls. Immunofluorescence analysis of spermatogenesis markers (PLZF, UCHL1, DDX4, PNA, Acrosin, PRM1) and blood-testis barrier integrity marker (β-catenin) confirmed that FMT from CD-treated mice induced histological changes similar to direct CD exposure (Figure S6).

Conversely, restoring normal microbiota to CD-treated mice (Group C) substantially rescued sperm parameters: sperm concentration, motile sperm percentage, and progressive motility approached control levels (no significant difference from controls), although straight-line velocity (VSL) remained reduced ((33.4±10.0) *vs.* (46.7±4.0) μm s^{-1}, P=0.038). Quantification of PLZF-positive spermatogonial stem cells revealed a significant 35.9% reduction in CD-treated mice (9.20±2.14 to 5.90±1.02 cells/tubule, P<0.001), which was partially restored by normal FMT (7.52±1.40 cells/tubule) (Figures S5 and S6).

CD-induced reproductive dysfunction shows partial reversibility after drug withdrawal

To assess reversibility, mice were maintained for 35 days (one complete spermatogenic cycle) after cessation of CD exposure. Compared with continuous CD treatment, the recovery group showed significant improvement in sperm motility (55.6% ±11.5% *vs.* 36.6%±10.6%, P=0.027) and rapid motility

(23.6%±2.9% *vs.* 18.6%±1.3%, P=0.014), with values approaching those of untreated controls. However, sperm concentration remained below control levels ((17.3±6.4)×10^6 *vs.* (27.4±7.4)×10^6 mL^{-1}, P=0.052), and PLZF-positive cell numbers showed partial but incomplete recovery (7.20±0.89 *vs.* 9.20±2.14 cells/tubule in controls) (Figures S5 and S6). These findings indicate that CD-induced reproductive toxicity is partially reversible, with sperm motility parameters recovering more rapidly than sperm concentration, suggesting that full recovery of spermatogenesis may require a longer period.

DISCUSSION

Over the past five decades, there has been a sharp decline in male fertility, with sperm concentration plummeting from 104 million per milliliter in 1973 to 49 million per milliliter in 2018, a decrease of 51.6%, making it one of the most alarming public health crises of our time (Levine et al., 2023). Although environmental toxins have long been considered the primary culprits behind this reproductive disaster, our research has uncovered a previously unrecognized threat: food-derived carbon nanodots (CDs) acting through novel gut-mediated mechanisms. This study provides integrative evidence that CDs can disrupt male reproductive function, primarily through a sequential cascade of gut microbiota dysbiosis, gut barrier dysfunction, systemic inflammation, and impaired blood-testis barrier integrity. Together, these findings highlight the gut-testis axis as a key pathway for dietary nanotoxicity.

The results indicate that CD exposure fundamentally reshapes the gut microbiome, characterized by a marked reduction in beneficial taxa such as *Akkermansia muciniphila* and *Acidaminococcus* spp. and an expansion of putative LPS-producing pathobionts, including Desulfovibrionaceae. This configuration is consistent with the emerging concept of the "androbactome," referring to gut microbiota and their genes that influence androgen biosynthesis and spermatogenesis (Kaltsas et al., 2025). Recent studies have confirmed that gut microbiota dysbiosis impairs male fertility through systemic inflammation, oxidative stress, endocrine disruption and epigenetic alterations, with LPS-driven cytokine production serving as a core mediating mechanism (Kaltsas et al., 2025). Although our data do not directly demonstrate how CDs interact with specific bacterial species, the observed restructuring strongly suggests that CDs perturb the intestinal ecosystem in a way that favours LPS-producing bacteria and disfavors barrier-supporting commensals. The underlying mechanisms are likely multifactorial, involving both direct nanoparticle-bacteria interactions and indirect changes in the intestinal microenvironment and barrier function (Fan et al., 2025; Zhang et al., 2025).

The selective bacterial effects observed in our study likely result from the differential antimicrobial properties of CDs. The physicochemical characteristics of CDs (surface charge: (−18.3±2.7) mV; size: (3.8±0.5) nm) enable membrane-directed antimicrobial activity with bacterial selectivity (Adhikari et al., 2013; Happy et al., 2018), while beneficial bacteria such as *Akkermansia muciniphila* are particularly sensitive to environmental stressors compared to resilient LPS-producing bacteria like *Desulfovibrio* species (Crawford et al., 2025; Wang et al., 2020b). This selective microbial disruption contributes to enhanced LPS biosynthesis, a common feature in metabolic disorders (Fallah and Mahdavi, 2023), linking our findings to the broader context of host-microbe metabolic dysregulation.

Consistent with this mechanistic interpretation, our functional metagenomic analysis revealed coordinated upregulation of the LPS biosynthesis pathway, with the expression of the rate-limiting enzyme LpxC increasing in a dose-dependent manner and positively correlating with the abundance of Desulfovibrionaceae and other putative pathobionts. Enhanced LPS biosynthesis and the resulting metabolic endotoxemia are well-recognized hallmarks of obesity, diabetes and related metabolic disorders, placing our findings within a broader framework of host-microbiota metabolic dysregulation and providing a mechanistic bridge between CD-induced gut dysbiosis and testicular inflammation along the gut-testis axis. Additionally, we observed significant inhibition of tryptophan metabolism, including reduced tryptophanase activity and decreased synthesis of protective indole metabolites, which are known to maintain intestinal barrier integrity via aryl hydrocarbon receptor (AHR) activation (Ranhotra, 2024; Scott et al., 2020).

The transition from gut microbiota dysbiosis to systemic toxicity is mediated by impaired gut barrier function, a phenomenon clearly confirmed by our metabolomics analysis. The convergence of gut and blood metabolite profiles in CD-exposed mice, distinct from the control group, provides strong evidence for increased gut permeability. This "leaky gut" phenotype was confirmed by histological examination, characterized by reduced mucus layer thickness and decreased expression of tight junction proteins, particularly occludin.

Tryptophan-derived indole metabolites play a key role in this barrier dysfunction. Indole-3-propionic acid and its related compounds enhance intestinal barrier function by strengthening epithelial tight junctions and mucus production (Li et al., 2021). The significant reduction in these protective metabolites following CD exposure creates favorable conditions for bacterial translocation. In parallel, our serum metabolomics data demonstrate a dose-dependent increase in arachidonic acid and other pro-inflammatory lipid mediators, accompanied by a decreasing trend in fecal arachidonic acid, consistent with enhanced luminal-to-systemic flux of this eicosanoid precursor (Guo et al., 2024b; Pan et al., 2024). Arachidonic acid-derived prostaglandins and leukotrienes can promote Th17/IL-17 responses and TLR4-dependent inflammatory signaling in peripheral tissues (Ołdak et al., 2024; Shao et al., 2024), providing a plausible mechanistic bridge between CD-induced gut dysbiosis, lipid metabolism dysregulation and the upregulation of testicular IL-17A and TLR4 observed in our study. The elevated levels of fecal endotoxin (LPS) we measured establish a complementary mechanistic link between microbial dysbiosis and systemic inflammation, consistent with findings that intestinal barrier dysfunction promotes endotoxin entry into the circulatory system (Taleb, 2019).

The BTB is a key regulatory point in the transition of systemic inflammation to reproductive dysfunction. This study demonstrates that LPS-mediated systemic inflammation significantly disrupts BTB integrity, manifested by reduced expression levels of key structural proteins (including N-cadherin, β-catenin, and occludin). This finding is consistent with recent studies showing that LPS exposure significantly downregulates the expression of BTB-related proteins and increases biotin permeability in the seminiferous tubules, with M1 polarization of testicular macrophages acting as a key mediator (Li et al., 2024a).

The underlying mechanisms involve LPS binding to Toll-like

https://doi.org/10.1007/s11427-025-3252-6

receptor 4 (TLR4) on the surface of immune cells, triggering the release of pro-inflammatory cytokines, which disrupt BTB integrity through oxidative stress and direct cytotoxic effects (Wang et al., 2019). Our transcriptomic analysis confirmed the significant upregulation of TLR4 and interleukin-17 receptor A (IL17RA), providing a molecular basis for LPS-mediated testicular inflammation. The role of the gut microbiota in this process has been supported by studies showing that antibiotic-induced gut microbiota dysbiosis exacerbates LPS-induced testicular inflammation and BTB dysfunction, and these effects can be reversed by fecal microbiota transplantation (Guo et al., 2024a).

We identified IL-17A as a key inflammatory mediator in CD-induced testicular dysfunction, consistent with the growing evidence of this cytokine's role in male reproductive pathology. Activation of the IL-17A signaling pathway is closely associated with spermatogenesis disorders. Studies have shown that environmental toxins such as glyphosate can induce gut microbiota dysbiosis, which in turn promotes IL-17A production in the testes and induces reproductive toxicity (Liu et al., 2022). The mechanism involves the migration of Th17 cells derived from gut microbiota to testicular tissue, where IL-17A activation triggers oxidative damage and disrupts spermatogenesis (Liu et al., 2022). Fluoride exposure studies provide additional mechanistic insights, indicating that IL-17A mediates testicular apoptosis via a caspase-1/11-dependent pathway, while IL-17A knockout mice exhibit protective effects against reproductive toxicity (Cheng et al., 2024). Our protein validation confirmed elevated IL-17A expression in testicular tissue following CD exposure, establishing this cytokine as a core mediator linking systemic inflammation to local reproductive dysfunction.

Time-series analysis revealed temporal relationships providing conclusive evidence for gut-mediated reproductive toxicity. Gut microbiota dysbiosis occurred within 1–3 days post-exposure, followed by disruption of Sertoli-germ cell communication and blood-testis barrier dysfunction (3–5 days), inflammatory activation (5–7 days), and reproductive dysfunction (after 7 days). This precise temporal sequence established causality and distinguished gut-mediated mechanisms from direct reproductive toxicity. Early downregulation of the gap junction protein GJB2 (connexin 26), which is essential for Sertoli-germ cell coupling but distinct from the tight junction proteins (Occludin, Claudins) that form the structural core of the Sertoli-Sertoli BTB, followed by delayed upregulation of TLR4 and IL17RA, indicates that impaired Sertoli-germ communication and BTB compromise precede inflammatory activation. This sequence aligns with the gut-testis axis concept, where intestinal barrier damage facilitates bacterial product translocation, thereby triggering testicular inflammation (Dubey et al., 2024). Recent studies on other environmental toxins, including liquid crystal monomers and polycyclic aromatic hydrocarbons, have also confirmed similar gut-mediated reproductive toxicity time patterns (Li et al., 2024b; Wu et al., 2025).

The antimicrobial properties of carbon nanomaterials, combined with their widespread presence in processed foods, make CDs a particularly concerning dietary contaminant. Exposure to CDs through processed foods, coupled with their gut-mediated reproductive toxicity, has profound implications for public health. Our dosing regimen is equivalent to a 70-kg individual consuming 464 mL–1.86 L of carbonated beverages daily, representing a realistic exposure scenario for many populations. The observed effects exhibit a dose-dependent pattern, indicating that even moderate intake levels may lead to reproductive dysfunction. The role of the gut microbiota as an environmental toxicity mediator opens new avenues for risk assessment and therapeutic interventions. Probiotic supplements have shown potential in mitigating reproductive toxicity induced by other environmental pollutants, with studies indicating that *Lactobacillus* strains can restore spermatogenesis in bisphenol A-exposed mice by regulating the gut microbiota (Wu et al., 2024). Similarly, the protective effects of beneficial bacterial metabolites (such as dipeptidyl glutamate produced by *Lactiplantibacillus plantarum*) have been reported (Juhász et al., 2024).

Although our mouse model provides valuable mechanistic insights, several limitations should be considered. The accelerated exposure protocol may not fully mimic the chronic low-level exposure pattern observed in humans. Additionally, interindividual variations in gut microbiota composition may significantly influence susceptibility to CD-induced toxicity, an aspect that requires further investigation in diverse populations. Importantly, our findings should not be interpreted to imply that all food-derived CDs are inherently toxic. As reviewed by Wang et al. (2020a), current research on food-borne CDs remains limited, and acute toxicity studies on CDs from carbonated beverages have shown negligible toxicity *in vivo* at high doses; however, investigations of chronic effects under realistic dietary exposure scenarios are insufficient. Our study contributes to this knowledge gap by demonstrating that prolonged exposure can induce reproductive toxicity through a microbiota-dependent mechanism. Whether F-CDs from other thermal processing methods with different physicochemical properties would produce similar effects requires further investigation.

CONCLUSION

This study identifies food-derived CDs as a novel class of potential reproductive toxicants and supports a mechanistic model in which an intestinal, microbiota-dependent pathway plays a predominant role. The sequential cascade from gut microbiota dysbiosis to testicular dysfunction (mediated by endotoxin (LPS) transport, systemic inflammation, and blood-testis barrier dysfunction) provides a new perspective on the mechanisms of dietary nanotoxicity. Our temporal analysis supports the gut-testis axis as the major pathway for CD-induced reproductive toxicity, while acknowledging that concurrent direct effects on testicular tissue cannot be fully excluded based on the present data, and highlights the critical role of the gut microbiota in mediating environmental health effects.

METHODS

In this study, we employed a comprehensive experimental approach to investigate the effects of carbon nanodots (CDs) in food on the gut-testicular axis (Figure 1A). The research workflow included CD separation and characterization, a 15-week chronic exposure model in mice, high-resolution time-series studies, and multi-omics analysis (transcriptomics, metagenomics, metabolomics) to elucidate the CD-induced reproductive toxicity mechanisms. The experimental design included reproductive toxicity assessment, gut microbiota profile analysis, metabolomics analysis, barrier function evaluation, and integrated pathway analysis to establish the time-series relationship between gut microbiota changes and testicular dysfunction.

Extraction and characterization of foodborne carbon dots

Source selection and isolation rationale

Carbonated beverages were selected as the CD source based on: (i) their detectable CD content (with extraction yields of ~3% from the beverage matrix (Li et al., 2018), (ii) their widespread consumption globally, particularly among reproductive-age populations, and (iii) their liquid matrix, which facilitates efficient CD extraction and standardization. CDs were extracted from a commercially available carbonated beverage (Coca-Cola®, lot No. 2023SZ01) following a previously validated protocol (Li et al., 2018) with modifications to optimize yield and purity.

Our extraction process consisted of four sequential steps: (i) concentration via rotary evaporation (40°C, 0.1 MPa; BUCHI R-300, Switzerland) to 5× the original concentration, (ii) removal of insoluble impurities by centrifugation (5,180×*g*, 30 min; Eppendorf 5910R, Germany), (iii) purification by sequential filtration through a 0.22-μm polyethersulfone membrane (Merck Millipore, USA) followed by D101 macroporous resin chromatography (Solarbio, Beijing, China), and (iv) dialysis of fluorescent fractions (1,000 D MWCO; BioFiven Inc., China) against ultrapure water for 48 h. We lyophilized (freeze-dried) the purified CDs (Christ Alpha 1-4 LDplus) and stored them at −80°C prior to characterization and animal exposure studies.

Physicochemical characterization

The isolated CDs were comprehensively characterized to confirm their identity and purity. Morphological analysis was performed by high-resolution transmission electron microscopy (HR-TEM, JEM-F200, JEOL) at 200 kV with size distribution analysis conducted across multiple fields (n=200 particles). For fluorescence spectroscopy, CDs were dissolved in ultrapure water at a concentration of 0.1 mg mL^{-1} and analyzed using an F-2700 fluorescence spectrophotometer (Hitachi, Japan) with excitation wavelengths scanned from 280 to 500 nm. UV-Vis absorption spectroscopy was performed on samples at the same concentration using a Lambda 35 spectrophotometer (PerkinElmer, USA). Surface charge and hydrodynamic size, critical parameters for biological interactions, were determined via dynamic light scattering (DLS; Malvern Zetasizer Nano ZS90) with measurements performed in triplicate at 25°C in physiological buffer (pH 7.4).

Animal experimental design

Male C57BL/6 mice (8 weeks old, representing human reproductive maturity, Gempharmatech Co.) were acclimatized for 7 days under controlled conditions (22°C±2°C, 55%±10% humidity, 12 h light/dark cycle). Following randomization using computer-generated random numbers, mice were assigned to three groups (n=10/group): Control (N): Standard AIN-93M diet without CD supplementation. LCD: AIN-93M diet supplemented with 25 mg kg^{-1} d^{-1} CDs. HCD: AIN-93M diet supplemented with 100 mg kg^{-1} d^{-1} CDs.

Dosages were established based on three principles: (i) correlation with documented human exposure levels, (ii) appropriate scaling between species, and (iii) consideration of the actual CD content in the original beverage matrix. Based on the reported CD extraction yield of approximately 3% from carbonated beverages (Li et al., 2018; Wang et al., 2015), and considering that Li et al. (2018) demonstrated the presence of fluorescent carbon nanoparticles (~5 nm) in commercial carbonated beverages that can be taken up by living cells, our dosing regimen was designed to reflect realistic human exposure scenarios.

We estimated realistic CD exposure from carbonated beverage consumption based on the extraction yields reported in the literature. Assuming typical daily consumption patterns, a 70 kg adult consuming 500 mL of carbonated beverage daily would be exposed to CDs at levels that, while not precisely quantified in foods, represent consistent dietary intake. Under high consumption scenarios (1.5 L d^{-1}), exposure could reach substantially higher levels. Given the limited quantitative data on CD concentrations in processed foods, we designed our experimental doses to encompass a range that would allow detection of potential adverse effects while remaining relevant to human consumption patterns.

Doses were calculated using body surface area (BSA) conversion to account for metabolic differences between mice and humans:

$$BSA_{mouse}=0.678\times\left(weight_{mouse}^{0.753}\right),$$

$$BSA_{human}=0.202\times\left(weight_{human}^{0.425}\right),$$

Conversion factor=$(BSA_{mouse}\div BSA_{human})=(km_{human}\div km_{mouse})=12.3$ (Nair and Jacob, 2016; Reagan-Shaw et al., 2008).

The human equivalent doses (HED) for our experimental groups were calculated as follows:

LCD (25 mg kg^{-1} d^{-1}): HED=25÷12.3=2.03 mg kg^{-1} d^{-1}.

HCD (100 mg kg^{-1} d^{-1}): HED=100÷12.3=8.13 mg kg^{-1} d^{-1}.

These experimental doses are consistent with standard toxicological practice of using doses several-fold higher than expected human exposure to detect potential adverse effects. The LCD represents a scenario of moderate exposure amplification suitable for detecting subtle effects, while the HCD provides a robust safety margin for identifying potential hazards. This dosing strategy ensures adequate sensitivity for detecting reproductive toxicity while maintaining relevance to human exposure patterns, particularly considering potential variations in individual consumption habits, CD content across different food products, and cumulative exposure from multiple dietary sources.

Time course study design

To establish a time series of CD-induced effects, a separate group of mice (6 mice per group, per time point) were administered CDs via oral gavage at the same dose as the HCD group (100 mg kg^{-1} d^{-1}) and euthanized on days 1, 3, 5, 7, and 13 post-initial exposure. Control mice received vehicle (ultrapure water) via oral gavage and were euthanized at the corresponding time points. CDs were administered daily via oral gavage throughout the exposure period until the designated euthanasia time point for each group. Fecal samples were collected daily for microbiome analysis, and testicular tissue was collected at each time point for transcriptomics analysis. All samples were immediately frozen in liquid nitrogen and stored at −80°C until analysis.

FMT experiments

To establish the causal role of gut microbiota in CD-induced reproductive toxicity, we performed bidirectional FMT experiments. Prior to FMT, all recipient mice underwent a 14-day antibiotic cocktail treatment to deplete the endogenous gut

https://doi.org/10.1007/s11427-025-3252-6

microbiota. The antibiotic cocktail consisted of ampicillin (1 g L^{-1}), neomycin (1 g L^{-1}), metronidazole (1 g L^{-1}), and vancomycin (0.5 g L^{-1}) administered in drinking water. Fresh fecal samples were collected from donor mice, homogenized in sterile PBS (100 mg feces mL^{-1}), and filtered through a 70-μm cell strainer. Following antibiotic washout (24 h), recipient mice received 200 μL of fecal suspension via oral gavage daily for 4 weeks. Two FMT groups were established (n=5 per group): (i) Group B (Normal+CD-FMT): normal mice receiving fecal microbiota from CD-treated donors; (ii) Group C (CD+Normal-FMT): CD-treated mice receiving fecal microbiota from normal healthy donors. Control Group A received a vehicle only, while Group E continued CD exposure without FMT.

Recovery experiment design

To assess the reversibility of CD-induced reproductive effects, a recovery group (Group D, n=5) was established. Mice received CD gavage (100 mg kg^{-1} d^{-1}) for 15 weeks following the same protocol as the HCD group, then were maintained for an additional 35 days without CD administration. This recovery period corresponds to approximately one complete spermatogenic cycle in mice, allowing sufficient time for potential regeneration of the spermatogenic lineage. At the end of the recovery period, mice were euthanized, and samples were collected for sperm parameter analysis and histological evaluation.

CASA

Sperm were collected from the cauda epididymis by mincing in pre-warmed HTF medium (37°C) and incubating for 15 min to allow sperm dispersal. Sperm parameters were analyzed using a Hamilton Thorne IVOS II computer-assisted sperm analyzer with the following settings: frame rate 60 Hz, frames acquired 30. Parameters measured included: total sperm concentration (×10^6 mL^{-1}), percentage of motile sperm, progressive motility (%), rapid motility (%), and kinematic parameters including average path velocity (VAP, μm s^{-1}), straight-line velocity (VSL, μm s^{-1}), and curvilinear velocity (VCL, μm s^{-1}). At least 200 sperm were analyzed per sample.

PLZF immunofluorescence quantification

To quantify spermatogonial stem cells, PLZF-positive cells were counted on immunofluorescence-stained testicular cross-sections. For each experimental group, at least 20 circular seminiferous tubule cross-sections were analyzed. PLZF-positive cells located along the basement membrane were counted manually using ImageJ software (NIH). Results are expressed as the mean number of PLZF-positive cells per tubule±SD. Additional spermatogenesis stage-specific markers (UCHL1, DDX4, PNA, Acrosin, PRM1, β-catenin) were analyzed to provide a comprehensive assessment of the spermatogenic lineage.

Reproductive toxicity assessment

Body weight and testicular morphology measurements

Body weight was monitored weekly during the 15-week exposure period. At the time of sacrifice, the testes were carefully dissected, photographed, and measured three times by a blinded observer to quantify the projected area of the testes.

Fertility testing

Male fertility was assessed via a mating experiment. After 15 weeks of CD exposure, male mice were co-housed with female C57BL/6 mice of proven fertility (male:female ratio 2:1) for 3 weeks. Pregnancy was confirmed by visual inspection and weight gain. Litter size was recorded at birth, and fertility was defined as the percentage of successful pregnancies per mating pair.

Testosterone and lipopolysaccharide measurement

After the mice were anesthetized, blood was taken from the eyeballs and centrifuged at 4°C and 3,000 r min^{-1} for 30 min to obtain serum. Serum testosterone levels were determined using a testosterone rat/mouse ELISA kit (Demeditec, Germany, Cat# DEV9911) following the manufacturer's instructions.

For the detection of LPS in fecal samples, the LPS ELISA Kit (FineTest, China, Cat#EU3126) was used according to the manufacturer's instructions. Dry mouse feces were added to PBS buffer, then subjected to ultrasonic pulverization, followed by centrifugation at 5,000×g to collect the supernatant for analysis.

Immunofluorescence staining

The specimens were sectioned at a thickness of 5 μm, sequentially deparaffinized, gradient dehydrated, and washed. After blocking with 5% bovine serum albumin at 37°C for one hour, the sections were incubated overnight at 4°C with primary antibodies. Next, the sections were exposed to fluorescently labeled goat anti-rabbit IgG secondary antibodies (1:100) at ambient temperature for one hour, rinsed with 4′,6-diamidino-2-phenylindole (DAPI) for 10 min, and mounted using an antifade solution. These steps were performed in a darkened environment, and fluorescence imaging was conducted with a Pannoramic 250FLASH scanner (3DHISTECH).

The primary antibodies used for immunofluorescence were against ACROSIN (Novus Biologicals, USA, CAT#NBP2-14260, 1:200), SCP3 (Abcam, UK, CAT#ab15093, 1:200), PRM1 (Proteintech, Wuhan, China, CAT#15697-1-AP, 1:200), DDX4 (Abcam, CAT#ab27591, 1:300), PNA (Thermo Fisher Scientific, USA, CAT#L21409, 20 μg mL^{-1}), StAR (CST, USA, CAT#D10H12, 1:200), and 3β-HSD (Santa Cruz, USA, CAT#sc-515120, 1:200).

Protein expression analysis

Testicular tissues were pulverized and sonicated before protein extraction using RIPA buffer (Cwbio, Taizhou, China). Protein concentrations were quantified via a BCA Protein Assay Kit (Thermo Fisher Scientific), which was used for subsequent sample preparation and electrophoresis for Western blot. The membranes were incubated with primary anti-PLZF antibody (1:1,000, sc-28319, Santa Cruz) overnight at 4°C, followed by incubation with secondary antibody (goat anti-rabbit/mouse IgG, 1:3,000, CST). Chemiluminescence imaging (Bio-Rad, USA) was used to visualize the signals.

Barrier function assessment

Intestinal barrier analysis

Intestinal tissue was processed as described above for histological analysis. Mucus layer thickness was measured using the Periodic Acid-Schiff (PAS) staining method according to standard

protocols. Tight junction protein analysis was performed by immunohistochemistry using anti-occludin antibodies.

Blood-testis barrier analysis

The integrity of the blood-testis barrier was assessed by immunohistochemical analysis of key tight junction proteins. The testis sections were deparaffinized, rehydrated, and subjected to endogenous peroxidase quenching with 3% H_2O_2. Antigen retrieval was followed by blocking with 5% goat serum. Primary antibodies were applied overnight at 4°C, followed by incubation with HRP-labeled secondary antibodies. DAB staining was used for visualization, and the sections were examined under a light microscope (Nikon, Japan).

The primary antibodies used for immunohistochemistry included antibodies against Occludin (Servicebio, Wuhan, China, CAT# GB111401, 1:800), β-catenin (Servicebio, CAT# GB15015, 1:1,000), N-cadherin (Servicebio, CAT# GB12135, 1:1,500), and IL-17a (Servicebio, CAT# GB11110-1, 1:700)

Metagenomic sequencing and analysis

Following protocols from prior studies (Chen et al., 2023), DNA was isolated (QIAamp® Fast DNA Mini Kit), quantified (NanoDrop2000), and integrity checked (agarose gel electrophoresis). Libraries, prepared with the TruSeq Nano DNA LT Sample Prep Kit, were sequenced on an Illumina NovaSeq 6000.

Data in FASTQ format were initially processed using fastp (v0.20.1) for adapter trimming and quality filtering, including the removal of reads with ambiguous bases (Chen et al., 2018). For host-associated DNA, bbmap (v38.93-0) was employed to align reads to the host genome and eliminate host sequences. The quality-controlled reads were then assembled into metagenomes with MEGAHIT (v1.2.9) (Li et al., 2015), and the ORFs predicted by Prodigal (v2.6.3) (Hyatt et al., 2010) were translated into amino acid sequences. A nonredundant gene set was constructed using MMSeqs2 (v13.45111) (Steinegger and Söding, 2017), with clustering based on 95% identity and 90% coverage. Gene abundance in the samples was quantified by aligning clean reads to this gene set using Salmon (v1.8.0). DIAMOND (v0.9.10.111) (Buchfink et al., 2015) facilitated the annotation of these sequences against databases including NR, KEGG, and GO, setting the BLAST *e*-value at 1×10^{-5} for taxonomic and functional annotations. R software (v4.1.2) was used for PCA and graphical representation of abundance profiles, along with PCoA and NMDS for distance matrix analysis, effectively condensing complex bioinformatic workflows into streamlined analyses of microbial communities and functional gene profiles.

To assess differential taxonomic and functional abundance between treatment groups, taxon- and pathway-level relative abundance tables were imported into R and compared across groups using Kruskal-Wallis tests for multi-group comparisons (Control, LCD, HCD or different time points). *P* values were adjusted for multiple testing using the Benjamini-Hochberg procedure, and taxa or pathways with an adjusted *P* value (false discovery rate, FDR) <0.05 were considered significantly differentially abundant unless otherwise specified.

Microbial co-occurrence network construction

The corAndPvalue function in WGCNA (Langfelder and Horvath, 2008) is used to calculate the Pearson correlation between species. Nodes with an absolute correlation coefficient greater than 0.4 and a BH-corrected *P*-value less than 0.05 are considered correlated. Network construction and visualization are carried out using igraph (Csárdi and Nepusz, 2006), with preprocessing of nodes before visualization, including the removal of unconnected nodes and self-referential nodes.

Integrated metabolomics

For differential metabolite abundance across treatment groups, $\log_{10}$-transformed peak intensities were compared using Kruskal-Wallis tests for multi-group comparisons (Control, LCD, HCD), followed where appropriate by pairwise post hoc testing. To control for multiple comparisons across metabolites, *P* values were adjusted by the Benjamini-Hochberg method, and metabolites with an FDR <0.05 were considered significantly altered. These criteria were applied consistently to both serum and fecal metabolomic datasets, including the focused analyses of arachidonic acid and purine/pyrimidine-related metabolites.

Serum and fecal metabolites were analyzed via liquid chromatography-tandem mass spectrometry (LC-MS/MS) using an ACQUITY UPLC I-Class Plus system coupled to a Xevo G2-XS QTOF mass spectrometer (Waters, USA). Samples were processed according to optimized protocols for each matrix type, with appropriate quality controls included. Data preprocessing, peak alignment, and normalization were performed using Progenesis QI. Metabolite identification was based on accurate mass, MS/MS fragmentation patterns, and retention time matching against the HMDB, METLIN, and in-house databases. Pathway enrichment and integration analyses were conducted using MetaboAnalyst 6.0 (Ewald et al., 2024).

Comprehensive transcriptomics analysis

Total RNA was extracted from testicular tissue using TRIzol reagent and quality assessed via Agilent 2100 Bioanalyzer (RIN>8.0). Library preparation and sequencing (Illumina NovaSeq 6000, 150 bp paired-end sequencing, 40 million reads per sample) were performed by OE Biotech Co., Ltd. (Shanghai, China).

Bioinformatics analysis included quality control, alignment of read sequences to the mm10 genome using HISAT2 (Kim et al., 2015), expression quantification using featureCounts, and differential expression analysis using DESeq2 (Love et al., 2014) (significance threshold: $|\log_2FC|>1$ and $P<0.05$). Gene filtering was performed to retain genes with total read counts $\geqslant10$ across all samples, or alternatively, genes with $\geqslant10$ reads in at least 3 samples to ensure adequate expression levels for statistical analysis. Sample grouping was performed based on treatment identifiers (Control, LCD, HCD) with proper factor level ordering. PCA and ternary plot analysis were performed using a custom R script to visualize treatment-specific expression patterns.

Cell type proportions in batch testis samples were estimated using cell type decomposition analysis. Macrophage polarization analysis was performed using an established M1/M2 gene signature. This tool was modified from CIBERSORT (Newman et al., 2019) and uses Support Vector Regression (SVR) for cell proportion estimation (https://github.com/chenpg2/CIBERSORT_GERM).

ClusterGVis was used to analyze gene expression trends to

identify co-expression clusters between different treatment groups. Functional enrichment analysis was performed using clusterProfiler combined with GO databases.

Statistical analysis and data integration

All quantitative data are presented as mean±standard error of the mean (SEM). Normal distribution was verified using the Shapiro-Wilk test. Intergroup comparisons were analyzed using one-way analysis of variance (ANOVA) followed by Tukey's post hoc test (GraphPad Prism 10.0) for normally distributed data, or using the Kruskal-Wallis test followed by Dunn's post hoc test for nonparametric data. Statistical significance was set at $P<0.05$.

Availability of data and material

The raw sequence data reported in this paper have been deposited in the Genome Sequence Archive in the China National Center for Bioinformation: Metagenome (CRA015550, https://ngdc.cncb.ac.cn/gsa/browse/CRA015550); Transcriptome (CRA015562, https://ngdc.cncb.ac.cn/gsa/browse/CRA015562); Metabolomics (OMIX006104, https://ngdc.cncb.ac.cn/omix/release/OMIX006104) (Chen et al., 2021; CNCB-NGDC Members and Partners, 2024). The codes used in this study can be obtained from the software author's GitHub, and no new code was generated.

Compliance and ethics

The authors declare that they have no conflict of interest. The experiment was approved by the Animal Ethics Committee of the Sixth Affiliated Hospital of Sun Yat-sen University (IACUC-2023102606, IACUC-2023032801) in accordance with the Guide for the Care and Use of Laboratory Animals.

Acknowledgement

This work was supported by the National Natural Science Foundation of China (81971759, 82171604, 22104157), Guangdong Basic and Applied Basic Research Foundation (2023B1515020108, 2023A1515110325), Guangdong Natural Science Foundation (2020A1515110774, 2023A151511099), Science and Technology Program of Guangzhou (202206010089), Shenzhen Science and Technology Program (RCBS20210706092410027), and Postdoctoral Fellowship Program of CPSF (GZC20233216). We thank OE Biotech Co., Ltd. (Shanghai, China) for assistance with the metabolomics sequencing used in this study.

Supporting information

The supporting information is available online at https://doi.org/10.1007/s11427-025-3252-6. The supporting materials are published as submitted, without typesetting or editing. The responsibility for scientific accuracy and content remains entirely with the authors.

References

Adhikari, M.D., Goswami, S., Panda, B.R., Chattopadhyay, A., and Ramesh, A. (2013). Membrane-directed high bactericidal activity of (gold nanoparticle)-polythiophene composite for niche applications against pathogenic bacteria. Adv Healthc Mater 2, 599–606.

Al-Asmakh, M., Stukenborg, J.B., Reda, A., Anuar, F., Strand, M.L., Hedin, L., Pettersson, S., and Söder, O. (2014). The gut microbiota and developmental programming of the testis in mice. PLoS One 9, e103809.

Buchfink, B., Xie, C., and Huson, D.H. (2015). Fast and sensitive protein alignment using DIAMOND. Nat Methods 12, 59–60.

Chen, P., Chen, H., Liu, Z., Pan, X., Liu, Q., and Yang, X. (2023). Fungal-bacteria interactions provide shelter for bacteria in Caesarean section scar diverticulum. eLife 12, RP90363.

Chen, S., Zhou, Y., Chen, Y., and Gu, J. (2018). fastp: an ultra-fast all-in-one FASTQ preprocessor. Bioinformatics 34, i884–i890.

Chen, T., Chen, X., Zhang, S., Zhu, J., Tang, B., Wang, A., Dong, L., Zhang, Z., Yu, C., Sun, Y., et al. (2021). The genome sequence archive family: toward explosive data growth and diverse data types. Genomics Proteomics Bioinf 19, 578–583.

Cheng, A., Luo, H., Fan, B., Xiang, Q., Nie, Z., Feng, S., Qiao, Y., Wu, Y., Zhu, Q., Liu, R., et al. (2024). Fluoride induces pyroptosis via IL-17A-mediated caspase-1/11-dependent pathways and *Bifidobacterium* intervention in testis. Sci Total Environ 926, 172036.

CNCB-NGDC Members and Partners. (2024). Database resources of the National Genomics Data Center, China National Center for Bioinformation in 2024. Nucleic Acids Res 52, D18–D32.

Cong, S., Bi, J., Song, X., Yu, C., and Tan, M. (2018). Ultrasmall fluorescent nanoparticles derived from roast duck: their physicochemical characteristics and interaction with human serum albumin. Food Funct 9, 2490–2495.

Crawford, M.S., Ulu, A., Ramirez, B.M., Santos, A.N., Chatterjee, P., Canale, V., Manz, S., Lei, H., Soriano, S.M., Nordgren, T.M., et al. (2025). Respiratory exposure to agriculture dust extract alters gut commensal species and key metabolites in mice. J Appl Toxicol 45, 1798–1810.

Csárdi, G., and Nepusz, T. (2006). The igraph software package for complex network research. InterJournal Complex Syst 1695.

Das, R., Kumar, A., Singh, C., and Kayastha, A.M. (2025). Innovative synthesis approaches and health implications of organic-inorganic nanohybrids for food industry applications. Food Chem 464, 141905.

Ding, N., Zhang, X., Zhang, X.D., Jing, J., Liu, S.S., Mu, Y.P., Peng, L.L., Yan, Y.J., Xiao, G.M., Bi, X.Y., et al. (2020). Impairment of spermatogenesis and sperm motility by the high-fat diet-induced dysbiosis of gut microbes. Gut 69, 1608–1619.

Dubey, I., K, N., G, V., Rohilla, G., Lalruatmawii, G., Naxine, P., P, J., Rachamalla, M., and Kushwaha, S. (2024). Exploring the hypothetical links between environmental pollutants, diet, and the gut-testis axis: the potential role of microbes in male reproductive health. Reprod Toxicol 130, 108732.

Esterházy, D., Canesso, M.C.C., Mesin, L., Muller, P.A., de Castro, T.B.R., Lockhart, A., ElJalby, M., Faria, A.M.C., and Mucida, D. (2019). Compartmentalized gut lymph node drainage dictates adaptive immune responses. Nature 569, 126–130.

Ewald, J.D., Zhou, G., Lu, Y., Kolic, J., Ellis, C., Johnson, J.D., Macdonald, P.E., and Xia, J. (2024). Web-based multi-omics integration using the Analyst software suite. Nat Protoc 19, 1467–1497.

Fallah, F., and Mahdavi, R. (2023). L-Carnitine and synbiotic co-supplementation: beneficial effects on metabolic-endotoxemia, meta-inflammation, and oxidative-stress biomarkers in obese patients: a double blind, randomized, controlled clinical trial. Food Funct 14, 2172–2187.

Fan, K., Tang, R., and Li, L. (2025). Characterization, antioxidant activity of banana peel carbon dots and their antibacterial mechanism against *Staphylococcus aureus*. J Appl Microbiol 136, lxaf163.

Guo, Q., Cheng, Y., Li, T., Huang, J., Li, J., Zhang, Z., and Qu, Y. (2024a). The gut microbiota contributes to the development of LPS-induced orchitis by disrupting the blood-testosterone barrier in mice. Reprod Sci 31, 3379–3390.

Guo, X., Xu, J., Zhao, Y., Wang, J., Fu, T., Richard, M.L., Sokol, H., Wang, M., Li, Y., Liu, Y., et al. (2024b). Melatonin alleviates heat stress-induced spermatogenesis dysfunction in male dairy goats by regulating arachidonic acid metabolism mediated by remodeling the gut microbiota. Microbiome 12, 233.

Gupta, R.K., Pipliya, S., Karunanithi, S., Eswaran U, G.M., Kumar, S., Mandliya, S., Srivastav, P.P., Suthar, T., Shaikh, A.M., Harsányi, E., et al. (2024). Migration of chemical compounds from packaging materials into packaged foods: interaction, mechanism, assessment, and regulations. Foods 13, 3125.

Happy, A., Soumya, M., Venkat Kumar, S., and Rajeshkumar, S. (2018). Mechanistic study on antibacterial action of zinc oxide nanoparticles synthesized using green route. Chem Biol Interact 286, 60–70.

Hyatt, D., Chen, G.L., LoCascio, P.F., Land, M.L., Larimer, F.W., and Hauser, L.J. (2010). Prodigal: prokaryotic gene recognition and translation initiation site identification. BMC Bioinform 11, 119.

Juhász, B., Horváth, K., Kuti, D., Shen, J., Feuchtinger, A., Zhang, C., Bata-Vidács, I., Nagy, I., Kukolya, J., Witting, M., et al. (2024). Dipeptide metabolite, glutamyl-glutamate mediates microbe-host interaction to boost spermatogenesis. Sci Rep 14, 21864.

Kaltsas, A., Giannakodimos, I., Markou, E., Stavropoulos, M., Deligiannis, D., Kratiras, Z., and Chrisofos, M. (2025). The androbactome and the gut microbiota-testis axis: a narrative review of emerging insights into male fertility. Int J Mol Sci 26, 6211.

Kim, D., Langmead, B., and Salzberg, S.L. (2015). HISAT: a fast spliced aligner with low memory requirements. Nat Methods 12, 357–360.

Langfelder, P., and Horvath, S. (2008). WGCNA: an R package for weighted correlation network analysis. BMC Bioinform 9, 559.

Levine, H., Jørgensen, N., Martino-Andrade, A., Mendiola, J., Weksler-Derri, D., Jolles, M., Pinotti, R., and Swan, S.H. (2023). Temporal trends in sperm count: a systematic review and meta-regression analysis of samples collected globally in the 20th and 21st centuries. Hum Reprod Update 29, 157–176.

Li, D., Liu, C.M., Luo, R., Sadakane, K., and Lam, T.W. (2015). MEGAHIT: an ultra-fast single-node solution for large and complex metagenomics assembly via succinct de Bruijn graph. Bioinformatics 31, 1674–1676.

Li, H., Hu, Y.F., Wang, X.R., Ouyang, K.W., Wang, H., Wang, K.W., Chang, W., Zhang, J., Yuan, Z., Xiong, Y.W., et al. (2024a). Suppressed testicular macrophage M1 polarization by HDAC5 enforces insensitivity to LPS-elicited blood-testis barrier

damage. Food Chem Toxicol 192, 114940.
Li, J., Zhang, L., Wu, T., Li, Y., Zhou, X., and Ruan, Z. (2021). Indole-3-propionic acid improved the intestinal barrier by enhancing epithelial barrier and mucus barrier. J Agric Food Chem 69, 1487–1495.
Li, S., Jiang, C., Wang, H., Cong, S., and Tan, M. (2018). Fluorescent nanoparticles present in Coca-Cola and Pepsi-Cola: physiochemical properties, cytotoxicity, biodistribution and digestion studies. Nanotoxicology 12, 49–62.
Li, Y., Ma, H., and Wang, J. (2024b). Effects of polycyclic aromatic hydrocarbons on the gut-testis axis. Ecotoxicol Environ Saf 280, 116539.
Liu, J.B., Chen, K., Li, Z.F., Wang, Z.Y., and Wang, L. (2022). Glyphosate-induced gut microbiota dysbiosis facilitates male reproductive toxicity in rats. Sci Total Environ 805, 150368.
Love, M.I., Huber, W., and Anders, S. (2014). Moderated estimation of fold change and dispersion for RNA-seq data with DESeq2. Genome Biol 15, 550.
Mandani, S., Dey, D., Sharma, B., and Sarma, T.K. (2017). Natural occurrence of fluorescent carbon dots in honey. Carbon 119, 569–572.
Nair, A.B., and Jacob, S. (2016). A simple practice guide for dose conversion between animals and human. J Basic Clin Pharm 7, 27.
Newman, A.M., Steen, C.B., Liu, C.L., Gentles, A.J., Chaudhuri, A.A., Scherer, F., Khodadoust, M.S., Esfahani, M.S., Luca, B.A., Steiner, D., et al. (2019). Determining cell type abundance and expression from bulk tissues with digital cytometry. Nat Biotechnol 37, 773–782.
Ołdak, M., Kurowska, W., Plebańczyk, M., Janicka, I., Radzikowska, A., Skalska, U., and Kuca-Warnawin, E. (2024). Adipose-derived mesenchymal stem cells from arthritis patients: differential modulation of $CD4^+$ T cell activation and cytokine production. Med Sci Monit 30, e945273.
Pan, Z., Luo, H., He, F., Du, Y., Wang, J., Zeng, H., Xu, Z., Sun, Y., and Li, M. (2024). Guava polysaccharides attenuate high fat and STZ-induced hyperglycemia by regulating gut microbiota and arachidonic acid metabolism. Int J Biol Macromol 276, 133725.
Ranhotra, H.S. (2024). Discrete interplay of gut microbiota L-tryptophan metabolites in host biology and disease. Mol Cell Biochem 479, 2273–2290.
Reagan-Shaw, S., Nihal, M., and Ahmad, N. (2008). Dose translation from animal to human studies revisited. FASEB J 22, 659–661.
Scott, S.A., Fu, J., and Chang, P.V. (2020). Microbial tryptophan metabolites regulate gut barrier function via the aryl hydrocarbon receptor. Proc Natl Acad Sci USA 117, 19376–19387.
Shao, A., Zhao, Q., and Chen, M. (2024). Homocysteine promotes intestinal inflammation in colitis mice through the PGE2/STAT3 signaling pathway. Dig Dis Sci 69, 3742–3752.
Sharma, M., Kumar, C., Arya, S.K., Puri, S., and Khatri, M. (2024). Neurological effects of carbon quantum dots on zebrafish: a review. Neuroscience 560, 334–346.
Singh, A.K., Itkor, P., Lee, M., Saenjaiban, A., and Lee, Y.S. (2024). Synergistic integration of carbon quantum dots in biopolymer matrices: an overview of current advancements in antioxidant and antimicrobial active packaging. Molecules 29, 5138.
Sk, M.P., Jaiswal, A., Paul, A., Ghosh, S.S., and Chattopadhyay, A. (2012). Presence of amorphous carbon nanoparticles in food caramels. Sci Rep 2, 383.
Song, Y., Cao, L., Li, J., Cong, S., Li, D., Bao, Z., and Tan, M. (2019). Interactions of carbon quantum dots from roasted fish with digestive protease and dopamine. Food Funct 10, 3706–3716.
Steinegger, M., and Söding, J. (2017). MMseqs2 enables sensitive protein sequence searching for the analysis of massive data sets. Nat Biotechnol 35, 1026–1028.
Taleb, S. (2019). Tryptophan dietary impacts gut barrier and metabolic diseases. Front Immunol 10, 2113.
Torres, P.J., Siakowska, M., Banaszewska, B., Pawelczyk, L., Duleba, A.J., Kelley, S.T., and Thackray, V.G. (2018). Gut microbial diversity in women with polycystic ovary syndrome correlates with hyperandrogenism. J Clin Endocrinol Metab 103, 1502–1511.
Wang, F., Liu, W., Jiang, Q., Gong, M., Chen, R., Wu, H., Han, R., Chen, Y., and Han, D. (2019). Lipopolysaccharide-induced testicular dysfunction and epididymitis in mice: a critical role of tumor necrosis factor alpha. Biol Reprod 100, 849–861.
Wang, H., Su, W., and Tan, M. (2020a). Endogenous fluorescence carbon dots derived from food items. Innovation 1, 100009.
Wang, Y., Yao, W., Li, B., Qian, S., Wei, B., Gong, S., Wang, J., Liu, M., and Wei, M. (2020b). Nuciferine modulates the gut microbiota and prevents obesity in high-fat diet-fed rats. Exp Mol Med 52, 1959–1975.
Wang, Z., Liao, H., Wu, H., Wang, B., Zhao, H., and Tan, M. (2015). Fluorescent carbon dots from beer for breast cancer cell imaging and drug delivery. Anal Methods 7, 8911–8917.
Wu, J., Lv, D., Lin, W., Mao, Y., Xia, Y., Feng, L., Zhao, T., Mao, X., Shu, F., and Guo, H. (2025). Chronic exposure to liquid crystal monomer EBCN at environmentally relevant concentrations induces testicular dysfunction via the gut-testis axis. J Hazard Mater 486, 137033.
Wu, J., Zhou, T., Shen, H., Jiang, Y., Yang, Q., Su, S., Wu, L., Fan, X., Gao, M., Wu, Y., et al. (2024). Mixed probiotics modulated gut microbiota to improve spermatogenesis in bisphenol A-exposed male mice. Ecotoxicol Environ Saf 270, 115922.
Zhang, B., Fan, X., Du, H., Zhao, M., Zhang, Z., Zhu, R., He, B., Zhang, Y., Li, X., Li, J., et al. (2023). Foodborne carbon dot exposure induces insulin resistance through gut microbiota dysbiosis and damaged intestinal mucus layer. ACS Nano 17, 6081–6094.
Zhang, C., Zheng, Y., Lin, X., and Weng, S. (2025). Research progress on the preparation, performance, mechanisms, and applications of carbon nanomaterials against Gram-negative bacteria. RSC Adv 15, 22180–22201.